

Construction of Donor–Acceptor Heterojunctions in Covalent Organic Framework for Enhanced CO₂ Electroreduction

Qiao Wu, Min-Jie Mao, Qiu-Jin Wu, Jun Liang, Yuan-Biao Huang,* and Rong Cao*

Covalent organic frameworks (COFs) are promising candidates for electrocatalytic reduction of carbon dioxide into valuable chemicals due to their porous crystalline structures and tunable single active sites, but the low conductivity leads to unmet current densities for commercial application. The challenge is to create conductive COFs for highly efficient electrocatalysis of carbon dioxide reduction reaction (CO₂RR). Herein, a porphyrin-based COF containing donor–acceptor (D–A) heterojunctions, termed TT-Por(Co)-COF, is constructed from thieno[3,2-b]thiophene-2,5-dicarbaldehyde (TT) and 5,10,15,20-tetrakis(4-aminophenyl)-porphinatocobalt (Co-TAPP) via imine condensation reaction. Compared with COF-366-Co without TT, TT-Por(Co)-COF displays enhanced CO₂RR performance to produce CO due to its favorable charge transfer capability from the electron donor TT moieties to the acceptor Co-porphyrin ring active center. The combination of strong charge transfer properties and enormous amount of accessible active sites in the 2D TT-Por(Co)-COF nanosheets results in good catalytic performance with a high Faradaic efficiency of CO (91.4%, –0.6 V vs reversible hydrogen electrode (RHE) and larger partial current density of 7.28 mA cm^{–2} at –0.7 V versus RHE in aqueous solution. The results demonstrate that integration of D–A heterojunctions in COF can facilitate the intramolecular electron transfer, and generate high current densities for CO₂RR.

1. Introduction

The ever-increasing energy demand by human society mainly depends on the burning of fossil fuels, which makes a substantial increase in atmospheric carbon dioxide (CO₂) concentration, leading to the intensification of the greenhouse effect and global warming.^[1] The efficient conversion of CO₂ into value-added chemicals has long aroused the interest of scientists worldwide for the carbon-neutral cycle.^[2–10] Among them, electrochemical carbon dioxide reduction (CO₂RR) using renewable electron energy with the advantages of being mild and clean, is a promising strategy to utilize CO₂ as a green C₁ feedstock sources to produce fuels and chemicals.^[11–17] However, the inert CO₂ usually leads to low current density and low energy conversion efficiency in the CO₂RR, which is not enough to meet the commercial applications. Thus, it is desirable to develop highly efficient electrocatalysts to improve the performance for CO₂RR.

Recently, porous crystalline materials, including metal-organic frameworks,^[18–22] and covalent organic frameworks (COFs),^[23–32] have received increasing attention in CO₂RR due to their high CO₂ adsorption affinity, accessible for the substrates to the isolated single-sites, and abundant of tunable active sites. Particularly, COFs connected by covalent bonds with robust reticular frameworks usually show high chemical stability, which can offer promising platforms for fabricating efficient electrocatalysts for CO₂RR.^[33,34] Moreover, a large number of active molecular catalyst such as cobalt porphyrin can be precisely integrated into the periodic array structures to obtain porous crystalline COFs with high surface areas for heterogeneous electrocatalytic CO₂ reduction. However, the majority of 2D COFs with poor electrical conductivity usually show very limited current densities and low energy conversion efficiency in CO₂RR. Hence, it is highly demanded to create conductive 2D COFs with efficient electron transfer ability to the integrated single active sites for CO₂RR in order to generate high current density.

To address this goal, we turned our attention to porphyrin-based 2D COFs with donor–acceptor (D–A) conjugations as a promising approach to increase the electron transfer rate. Sulfur-containing aromatic heterocycles and their derivatives, as a class of excellent electron donors with high electron mobility, have been widely used to synthesize highly conductive

Q. Wu, M.-J. Mao, Q.-J. Wu, Prof. Y.-B. Huang, Prof. R. Cao
 State Key Laboratory of Structural Chemistry
 Fujian Institute of Research on the Structure of Matter
 Chinese Academy of Sciences
 Fuzhou 350002, China
 E-mail: ybhuang@fjirms.ac.cn; rcao@fjirms.ac.cn

Q. Wu, Prof. R. Cao
 Department of Chemistry
 College of Chemistry and Chemical Engineering
 Xiamen University
 Xiamen 361005, China

Q. Wu, M.-J. Mao, Prof. Y.-B. Huang, Prof. R. Cao
 Fujian College
 University of Chinese Academy of Sciences
 Fuzhou 350002, China

Dr. J. Liang
 Hoffmann Institute of Advanced Materials
 Shenzhen Polytechnic
 Shenzhen 518055, China

Prof. Y.-B. Huang, Prof. R. Cao
 University of Chinese Academy of Sciences
 Beijing 100049, China

 The ORCID identification number(s) for the author(s) of this article can be found under <https://doi.org/10.1002/smll.202004933>.

DOI: 10.1002/smll.202004933

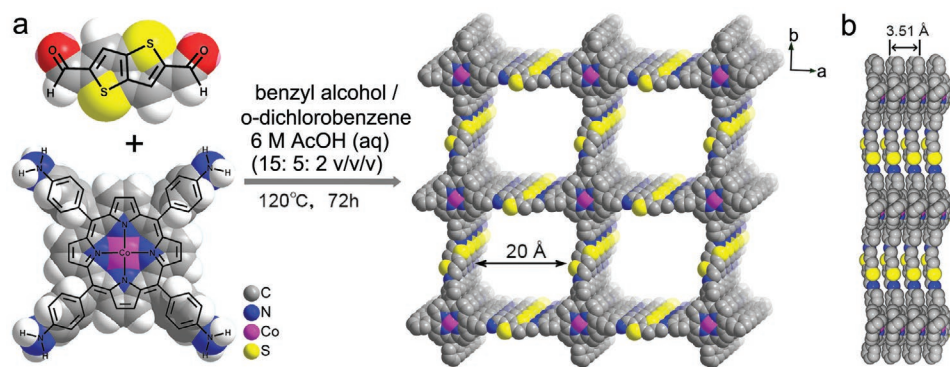


Figure 1. a) Schematic synthesis of 2D TT-Por(Co)-COF, featuring tetragonal pores with a diameter of 2.0 nm. b) Illustration of TT-Por(Co)-COF networks stacked along the *c* axis, showing the interlayer distance of 3.51 Å.

charge transfer materials when being combined with molecules as electron acceptors.^[35–42] Metalloporphyrin has a conjugated electron system and can be used as an excellent electron acceptor or electron transfer carrier.^[43–45] Moreover, porphyrins generally have small highest occupied molecular orbital and lowest unoccupied molecular orbital (HOMO–LUMO) gaps that can easily allow uptake and release of electrons, leading to fast electron transfer to reactant substrates and enhance activities.^[46] Thus, the covalent connection of sulfur-containing aromatic heterocycles and metalloporphyrins active sites to construct D–A conjugation system in a COF would be an effective strategy to improve intramolecular charge transfer capacity to enhance the energy conversion efficiency of CO₂RR.

The integration of a well-defined electron-rich thieno[3,2-*b*]thiophene-2,5-dicarbaldehyde (TT) monomer (Figure 1a) and metalloporphyrin units into the architectures of a 2D COF with unique D–A heterojunctions would thus be expected, in which highly efficient electronic transmission paths could be made to enhance electrocatalytic CO₂RR performance. Herein, we constructed D–A heterojunctions in a porous crystalline 2D Coporphyrin-based COF (TT-Por(Co)-COF), in which thieno[2,3-*b*]thiophene-based building blocks serving as electron donors, while Co-porphyrins as electron acceptors. Thus, TT-Por(Co)-COF has shown fast electron transfer ability as verified by the carrier mobility measurements, electrochemical impedance spectroscopy (EIS), and conductivity measurements. Moreover, the 2D TT-Por(Co)-COF could be easily exfoliated to nanosheets with three- to four-layers by ultrasonic treatment, thus an abundant of Co active sites can be exposed to the electrolytes and CO₂. Due to its good charge transfer ability and large number of accessible active sites, TT-Por(Co)-COF nanosheets exhibited high CO selectivity with Faraday efficiency up to 91.4% at the potential of –0.6 V versus reversible hydrogen electrode (RHE) and larger partial current density of 7.28 mA cm^{–2} at –0.7 V versus RHE in aqueous solution, which is higher than COF-366-Co with partial current density of 2.89 mA cm^{–2} at the same potential.

2. Results and Discussion

The 2D TT-Por(Co)-COF was synthesized via a solvothermal Schiff-base condensation reaction of 5,10,15,20-tetrakis(4-

aminophenyl)-porphyrinatocobalt (Co-TAPP) and thieno[3,2-*b*]thiophene-2,5-dicarbaldehyde (TT) with 1:2 molar ratio in a solvent mixture of benzyl alcohol, *o*-dichlorobenzene and 6 M acetic acid (15:5:2, v:v:v) at 120 °C for 72 h (Figure 1a). For comparison, we also prepared the metal-free TT-Por(2H)-COF (Figure S1, Supporting Information) with TAPP monomer instead of Co-TAPP under similar conditions (Figure S2, Supporting Information).^[47] To investigate the role of TT in TT-Por(Co)-COF, the COF-366-Co (Figure S3, Supporting Information) with 1,4-benzenedicarbaldehyde (BDA) instead of TT was also prepared according to the reported method.^[23] The powder X-ray diffraction (PXRD) patterns (Figure 2a) showed intense peaks in low 2θ angles range of TT-Por(Co)-COF, with no residual peaks characteristic of the starting materials. The triclinic *P1* space group was built by Materials Studio, and Pawley refinements of the XRD patterns was carried out for full profile fitting against the proposed models, which provided a unit cell parameter of $a = 26.34$ Å, $b = 25.60$ Å, $c = 5.09$ Å, and $\alpha = 115.69^\circ$, $\beta = 89.79^\circ$, $\gamma = 90.88^\circ$. The weighted-profile *R* factor (R_{wp}) is 6.02% and unweighted-profile *R* factor (R_p) is 4.67%, which indicate reasonable profile differences. TT-Por(Co)-COF has intense PXRD peaks at 3.38, 6.67, and 7.63°, which are assigned to the (100), (200), and (020) facets, respectively. The simulated PXRD patterns were consistent with the experimental results. These refinements reveal that there is 1D channel along *c* axis with the theoretical pore sizes of 2.0 nm, and the distance between adjacent stacking 2D sheets is 3.51 Å (Figure 1).

The Fourier transform infrared spectroscopy (FT-IR) in Figure 2b shows that the C=N imine stretching vibration band at 1583 cm^{–1} appeared in the TT-Por(M)-COF (M=Co, 2H) materials, while the C=O stretching vibration band at 1653 cm^{–1} belonged to the TT monomer disappeared after polymerization, confirming the formation of the imine bonds as well as the completeness of the Schiff-base condensation reaction.^[47] Moreover, the newly formed C=N bonds (chemical shift values at 146.8 ppm for TT-Por(Co)-COF and 147.8 ppm for TT-Por(2H)-COF) were also verified by solid-state ¹³C NMR spectra (Figures S4 and S5, Supporting Information),^[47] which further confirmed the successful condensation reaction for the formation of TT-Por(M)-COF (M=Co, 2H). Inductively coupled plasma (ICP) optical emission spectrometry demonstrated that TT-Por(Co)-COF had a high Co content of 4.16 wt%, suggesting

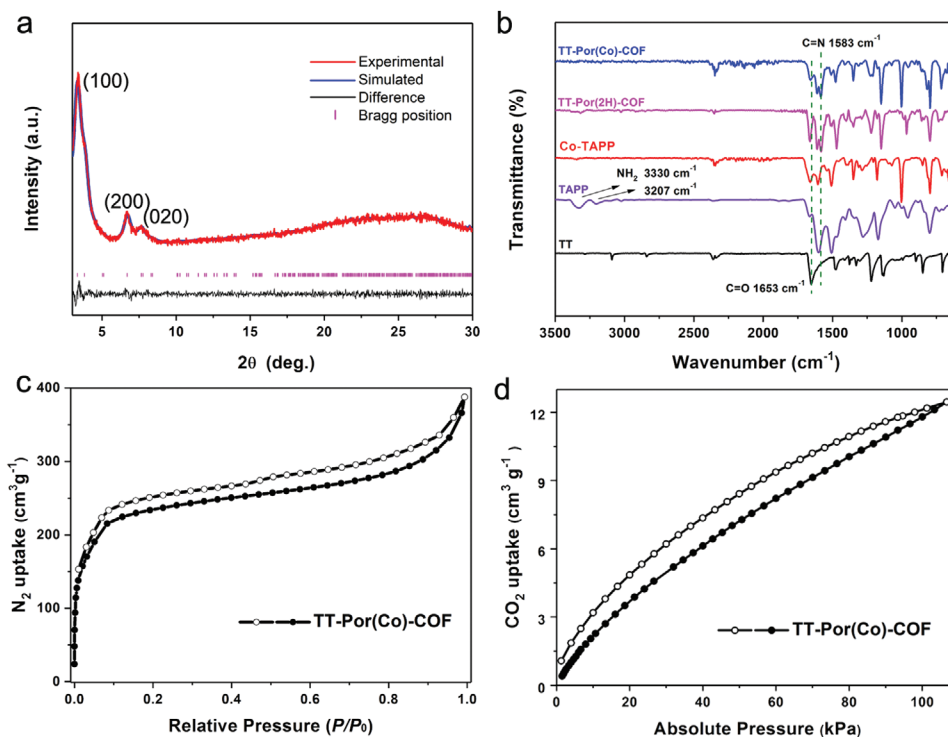


Figure 2. a) Experimental (red) and simulated (blue) PXRD patterns of TT-Por(Co)-COF. b) Comparison of FT-IR spectra of TT-Por(Co)-COF and TT-Por(2H)-COF with the TT, TAPP, and Co-TAPP monomer. c) N₂ adsorption curve at 77 K and d) CO₂ adsorption curve at 298 K for TT-Por(Co)-COF.

high number of Co-porphyrin active sites have been inserted in the framework. The elemental analysis (EA) revealed that the contents of S and N were 8.37 and 9.86 wt%, respectively, further indicating that TT and Co-porphyrin motifs are existed in TT-Por(Co)-COF.

N₂ and CO₂ isotherms were collected to investigate the porosity nature and CO₂ affinities of TT-Por(M)-COF (M=Co, 2H) materials. The N₂ isotherms at 77 K showed that TT-Por(Co)-COF has a high Brunauer–Emmett Teller (BET) surface area of 748 m² g⁻¹ and a pore volume of 0.60 cm³ g⁻¹ (Figure 2c). The pore size distribution analysis revealed that the pore range of TT-Por(Co)-COF located between 1.2 and 1.9 nm (Figure S6, Supporting Information), which is in agreement with the simulated pore size of 2.0 nm along *c* axis (Figure 1a). On the other hand, TT-Por(2H)-COF showed similar results with a slightly lower BET surface area of 628 m² g⁻¹ and pore sizes centered at 1.1 and 2.2 nm (Figure S7, Supporting Information). Furthermore, the CO₂ uptake values for TT-Por(Co)-COF and TT-Por(2H)-COF were 12 and 14 cm³ g⁻¹, respectively (Figure 2d; Figure S8, Supporting Information), which would be beneficial for promoting CO₂RR performance.

The scanning electron microscopy images show that TT-Por(Co)-COF are composed of sheet-like layered structure (Figure S9, Supporting Information), which is supported by the transmission electron microscopy image (TEM) (Figure 3a). The high-resolution TEM (HR-TEM) image of TT-Por(Co)-COF (Figure 3a) displays crystal ordered pore channels with lattice fringe spacing of 2.2 nm, which is consistent with the pore size of simulated network (Figure 1a). The fast Fourier transform patterns of yellow box field in Figure 3a

displays polycrystalline structure composed of sheets, which also confirms the successful formation of crystalline ordered TT-Por(Co)-COF. Besides, the energy-dispersive X-ray spectroscopy (EDS) elemental mapping images demonstrate that C, N, S, and Co elements are uniformly distributed in TT-Por(Co)-COF (Figure 3b), which is consistent with EA and ICP tests. To guarantee those porphyrin cobalt active sites in the TT-Por(Co)-COF layers could be effectively exposed to the electrolytes and CO₂, the 2D TT-Por(Co)-COF material with thinner sheets were prepared by exfoliation under high-frequency sonication at room temperature. As shown by atomic force microscopy (AFM) image in Figure 3c, thickness of about 1.3 nm can be clearly seen, which is corresponding to three- to four-layer TT-Por(Co)-COF nanosheets (Figure 3d). Such ultrathin 2D TT-Por(Co)-COF nanosheets would be beneficial for the accessible Co active sites for electrolytes and CO₂.

To further confirm the electronic and coordination structure of the cobalt species in TT-Por(Co)-COF, X-ray absorption spectroscopy was performed. The X-ray absorption near-edge structure (XANES) of Co *K*-edge (Figure 4a) located between those of CoO and Co foil, implying the positive charged cobalt is between Co(0) and Co(II) in TT-Por(Co)-COF. Furthermore, a weak pre-edge peak at 7115 eV is observed, which is recognized as the 1s→4p_z shake-down transition and suggests the existence of Co-N₄ square-planar structure.^[48] The Co *K*-edge of extended X-ray absorption fine structure (EXAFS) shows a main signal at 1.50 Å assigned to the Co–N scattering path (Figure 4b), which is similar to that of [5,10,15,20-tetrakis(4-cyanophenyl)porphyrinato]-Co (Co-TPPCN, 1.47 Å).^[49] More importantly, no obvious signals ascribed to Co–Co (2.17 Å) can be detected,

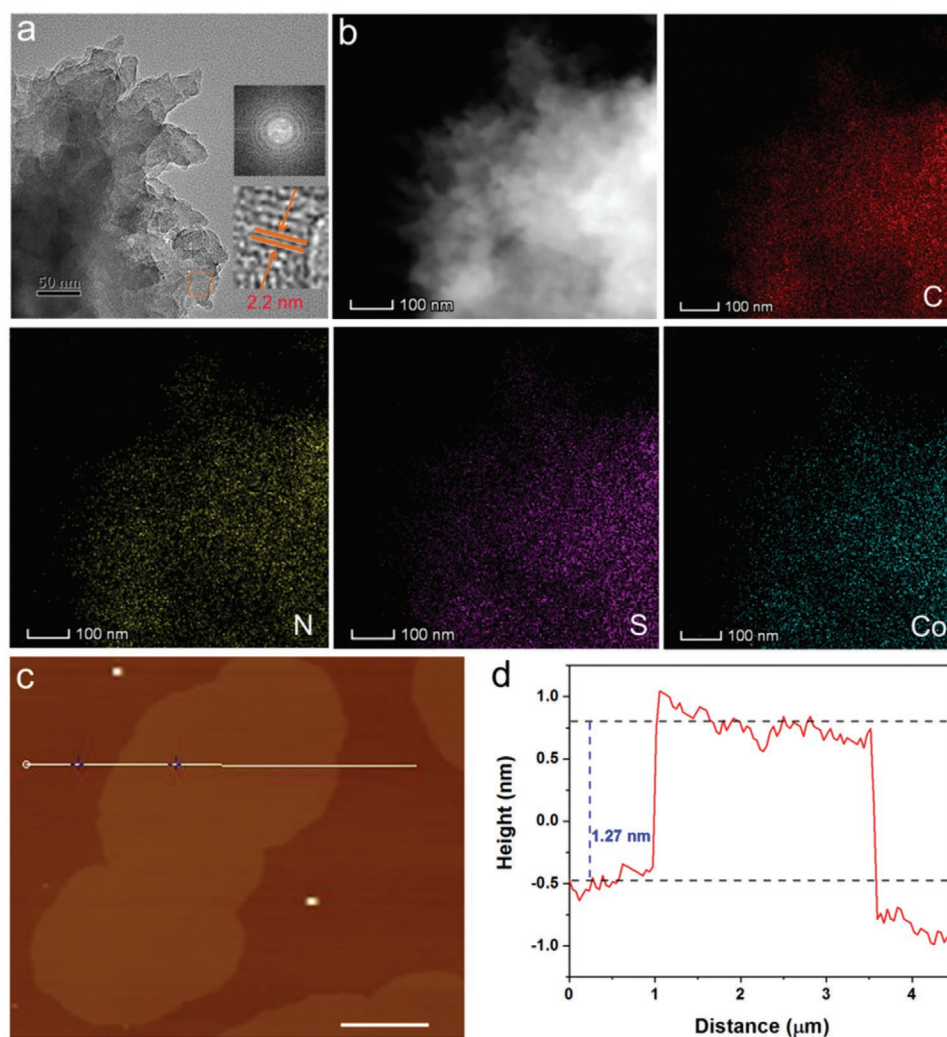


Figure 3. a) TEM image of TT-Por(Co)-COF (Inset: HR-TEM image and the fast Fourier transformation and the lattice distance), and b) the corresponding HAADF-STEM and EDS mapping of C, N, S, and Co elements in of TT-Por(Co)-COF. c) The atomic force microscope image (AFM) of TT-Por(Co)-COF sheets, scale bar is 1 μm . d) The height profile of AFM along the marked white line of TT-Por(Co)-COF sheets.

further revealing that atomic Co-N_x species are predominated and Co, CoO , and Co_3O_4 particles are not detected in TT-Por(Co)-COF. In order to determine the Co coordination environment, the fitting results from EXAFS show that the coordination number of Co species in TT-Por(Co)-COF is calculated to be 4.0 (Figure 4c; Table S1, Supporting Information), suggesting that the Co porphyrin structure is retained.

To investigate superiority of TT-Por(Co)-COF over COF-366-Co without TT unit for the electron-transfer behavior in electrocatalytic CO_2RR , the conductivity measurements were performed in air using the powder pellet two-electrode method (Figure S10, Supporting Information). Interestingly, the TT-Por(Co)-COF has a two times higher electron conduction value ($1.38 \times 10^{-8} \text{ S m}^{-1}$) than that of COF-366-Co ($6.5 \times 10^{-9} \text{ S m}^{-1}$),^[50] indicating that the D–A heterojunctions play an important role in promoting charge transfer. The results also suggest that an oriented electron pathway could have been created from the strong electron donor TT to the acceptor Co-TAPP in 2D TT-Por(Co)-COF. The current–voltage curves

(Figure S11, Supporting Information) show that the carrier mobility (μ) of TT-Por(Co)-COF ($0.18 \text{ cm}^2 \text{ V}^{-1} \text{ s}^{-1}$) is higher than that of COF-366-Co ($0.06 \text{ cm}^2 \text{ V}^{-1} \text{ s}^{-1}$),^[50] which could be attributed to the electron transfer from the TT units to the cobalt porphyrin rings. In addition, EIS tests show that TT-Por(Co)-COF has smaller semicircle than COF-366-Co (Figure S12, Supporting Information), which is in agreement with conductivity measurements.

To further confirm that the charge transfer from the electron donor of TT moieties to electron acceptor Co porphyrin in TT-Por(Co)-COF, cyclic voltammetry curve and solid state UV spectra measurements were conducted. We calculated and discussed LUMO and HOMO of the monomers (Figure S13–S15, Supporting Information). The electrochemical tests provided the oxidation and reduction potentials of electroactive linker molecules. As shown in Figure S13, Supporting Information, we obtained the first oxidation waves ($E^{\text{OX}} = 0.95 \text{ V}$) of Co-TAPP and TT fragment ($E^{\text{OX}} = 1.16 \text{ V}$) by differential pulse voltammetry (DPV) tests. The potential

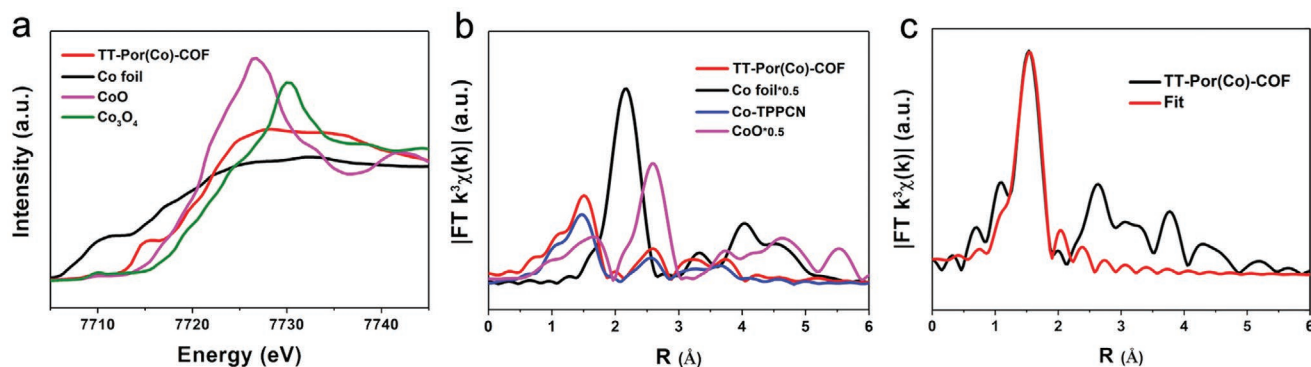


Figure 4. a) Co *K*-edge of XANES spectra of TT-Por(Co)-COF, Co foil, CoO, and Co₃O₄. b) Co *K*-edge of EXAFS spectra of TT-Por(Co)-COF, Co-TPPCN, and CoO. c) The EXAFS fitting curves of TT-Por(Co)-COF.

of $E(\text{Fc}/\text{Fc}^+) = -4.80$ eV versus E_{vac} (vacuum conditions) was obtained when ferrocene (Fc) was used as internal reference.^[51] The Tauc plots of solid-state UV spectra (Figure S14, Supporting Information) show that the band gaps (E_g) for TT fragment and Co-TAPP are 2.04 and 1.66 eV, respectively. The relative positions of HOMO and LUMO were obtained according to the formula ($\text{HOMO} = -[eE^{\text{OX}} - eE(\text{Fc}/\text{Fc}^+) + 4.8 \text{ V}]$) eV, $\text{LUMO} = \text{HOMO} - E_g$.^[45] The LUMO of TT possesses higher potential (-3.47 eV) than Co-TAPP (-3.64 eV), which is sufficient to realize the electron transfer from TT to Co-TAPP (Figure S15, Supporting Information). This is also confirmed by an apparent change of bonding energies of Co and S in TT-Por(Co)-COF, compared with those in Co-TAPP and TT monomers. The X-ray photoelectron spectroscopy (XPS) of Co_{2p} revealed that the binding energies of the cobalt species in TT-Por(Co)-COF (780.31 eV for 2p_{3/2} and 795.60 eV for 2p_{1/2}) were lower than those of Co-TAPP (780.98 eV for 2p_{3/2} and 796.03 eV for 2p_{1/2}) (Figure S16a, Supporting Information). While the bonding energy (164.33 eV, 2p_{3/2}) of sulfur in TT-Por(Co)-COF (Figure S16b, Supporting Information) was higher than that of sulfur in TT monomer (163.96 eV, 2p_{3/2}). The XPS results suggest the presence of charge carrier migration pathway from TT to porphyrin cobalt center in TT-Por(Co)-COF. In addition, compared with the solid-state UV spectrum of COF-366-Co, a red-shift phenomenon for TT-Por(Co)-COF with strong molecular D–A heterojunctions was observed (Figure S17, Supporting Information),^[52] which was attributed to the electron transfer behavior in TT-Por(Co)-COF.

The strong electron transfer ability and abundant accessible Co active sites in the TT-Por(Co)-COF nanosheets with D–A heterojunctions motivated us to investigate their electrocatalytic CO₂RR performances. The CO₂RR performances for TT-Por(Co)-COF were tested in a three-electrode electrochemical H-type cell with a cathodic compartment and an anodic compartment separated by a Nafion-117 proton exchange membrane. The linear sweep voltammetry (LSV) curves (Figure 5a; Figure S18, Supporting Information) demonstrate that TT-Por(Co)-COF and COF-366-Co have much larger current densities in CO₂-saturated than in Ar-saturated 0.5 M KHCO₃ solution, indicating higher reaction activity of electrocatalytic CO₂RR than hydrogen evolution reaction (HER). Gas chromatography (GC) analysis revealed that the main gas products was CO or H₂ (Figure 5b; Figure S19, Supporting Information)

and there was no liquid product based on ¹H NMR spectroscopy analysis (Figure S20, Supporting Information). It should be noted that CO was not produced when the electrocatalysis was conducted under Ar-saturated atmosphere (Figure S21, Supporting Information), further confirming their activities originated from CO₂ reduction. As shown in Figure 5b, TT-Por(Co)-COF exhibited a high Faradaic efficiency (FE_{CO}) of 91.4% at -0.6 V versus RHE, which was higher than that of COF-366-Co (67.3%) at the same potential and other reported COFs (Table S2, Supporting Information). With the increase of potential, the CO partial current density of TT-Por(Co)-COF continuously increased and reached up to a maximum value of 7.28 mA cm⁻² at -0.7 V versus RHE, which is 2.5 times that of COF-366-Co (2.89 mA cm⁻²) (Figure 5c) and is higher than other reported COFs in terms of the CO partial current density (Figure S22, Supporting Information).^[23,33,45,50] Such excellent CO₂RR performance of TT-Por(Co)-COF highlights the effectiveness merging D–A electron heterojunctions into the network.

To confirm the active sites of TT-Por(Co)-COF, we measured the TT-Por(2H)-COF without cobalt or ketjenblack for the catalytic CO₂RR under the same conditions. As shown in Figures S23–S24, Supporting Information, TT-Por(2H)-COF showed negligible catalytic activities for CO₂RR and only HER happened at various applied potentials. In addition, ketjenblack exhibited almost 100% Faradaic efficiency (FE_{H_2}) at -0.9 to -1.1 V versus RHE, which indicated the inability of ketjenblack for CO₂RR (Figure S25, Supporting Information). These results indicated the important role of cobalt centers in TT-Por(Co)-COF for the CO₂-to-CO conversion. The results indicating that important role of cobalt centers of TT-Por(Co)-COF for the CO₂-to-CO conversion. To estimate the electrochemical active surface area, cyclic voltammetry tests of TT-Por(Co)-COF and COF-366-Co are conducted (Figure S26, Supporting Information). The results indicated that TT-Por(Co)-COF (2.64×10^{-9} mol) and COF-366-Co (2.09×10^{-9} mol) have almost active sites. However, compared with COF-366-Co without TT, TT-Por(Co)-COF has a higher FE_{CO} of 91.4% at -0.6 V versus RHE, which is attributed to the efficient electron transfer from TT to porphyrin cobalt center in TT-Por(Co)-COF. Moreover, TT-Por(Co)-COF showed an acceptable turnover frequency (TOF) of 481 h⁻¹ based on Co center at -0.7 V versus RHE (Figure S27, Supporting Information).

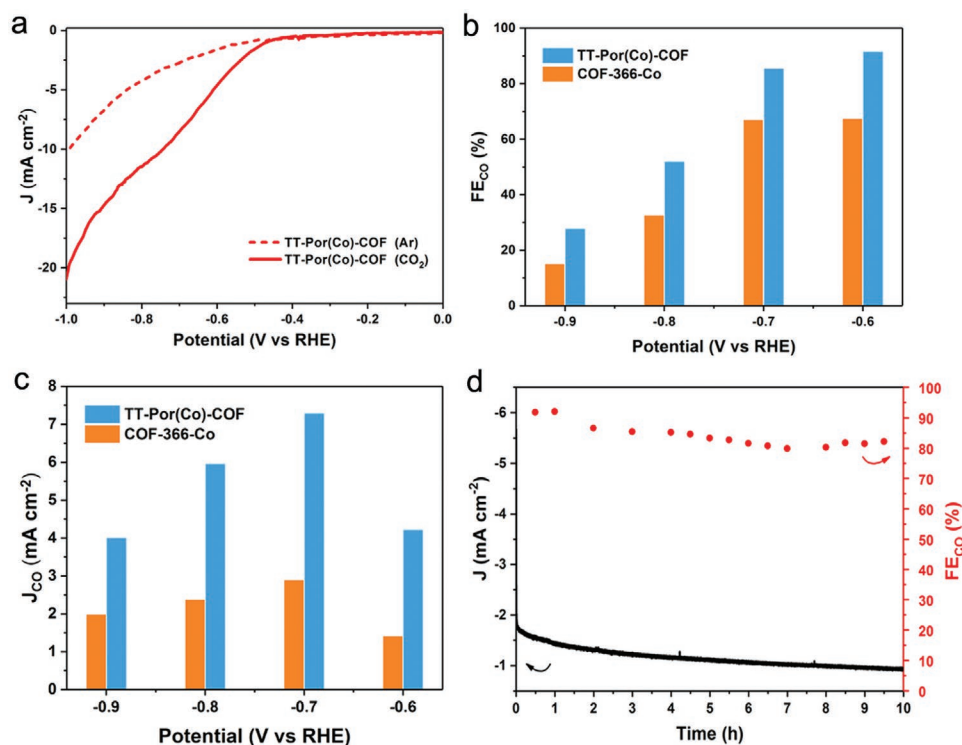


Figure 5. a) LSV curves in CO_2 -saturated and Ar-saturated 0.5 M KHCO_3 at a scan rate of 10 mV s^{-1} . b) FE_{CO} and c) J_{CO} from -0.6 to -0.9 V versus RHE of TT-Por(Co)-COF and COF-366-Co. d) Stability test of TT-Por(Co)-COF in CO_2 -saturated 0.5 M KHCO_3 electrolyte at a potential of -0.6 V versus RHE during 10 h.

To study the long-term stability of TT-Por(Co)-COF, the electrocatalyst was performed with chronoamperometric test at a fixed potential of -0.6 V versus RHE in CO_2 -saturated 0.5 M KHCO_3 solution. After 10 h, the corresponding FE_{CO} can be retained at values above 80% over the entire experiment (Figure 5d). Compared with the fresh catalyst, significant change on the Co *K-edge* of TT-Por(Co)-COF after electrolysis at -0.6 V was not observed (Figures S28–S29, Supporting Information), indicating that the coordination environments of most cobalt centers were remained. Besides, the ICP result of TT-Por(Co)-COF after long-time durability test ruled out leaching of Co species from the framework, which is in agreement with the negligible metal ions in the electrolyte. Moreover, the XPS curves (Figure S30, Supporting Information) after electrocatalysis showed that bonding energies at 780.29 and 795.12 eV are responsible for $2p_{3/2}$ and $2p_{1/2}$, respectively, corresponding to the valence state of Co^{2+} . Therefore, the gradual decrease in current density during the long-time durability is probably not caused by the structure change of TT-Por(Co)-COF. The decrease in current density could be connected with the hydrogenation on the pyrrole rings of porphyrin under a protic and reductive environment, which is also noticed previously in cobalt phthalocyanine^[53] and nickel-porphyrin systems.^[54,55]

3. Conclusion

In summary, D–A heterojunctions were constructed in a 2D cobalt porphyrin-based COF (TT-Por(Co)-COF) that was obtained

by a Schiff-base reaction of thieno[3,2-*b*]thiophene-2,5-dicarbaldehyde (TT) and Co-TAPP to enhance the electrocatalytic performance of CO_2RR via improving charge transfer ability. TT-Por(Co)-COF has a good electron conduction value ($1.38 \times 10^{-8} \text{ S m}^{-1}$) and carrier mobility value ($0.18 \text{ cm}^2 \text{ V}^{-1} \text{ s}^{-1}$). Moreover, the LUMO of TT possesses higher potential (-3.47 eV) than Co-TAPP (-3.64 eV), which is beneficial to realize the electron transfer from TT to porphyrin cobalt center in TT-Por(Co)-COF. In addition, compared with COF-366-Co, a red-shift phenomenon for TT-Por(Co)-COF was observed in solid-state UV spectrum, which was attributed to the electron transfer behavior in TT-Por(Co)-COF. As a result, compared with COF-366-Co without TT, TT-Por(Co)-COF is able to selectively convert CO_2 -to-CO with a high FE_{CO} of 91.4% at -0.6 V versus RHE and larger partial current density of 7.28 mA cm^{-2} at -0.7 V versus RHE in aqueous solution. This work provides a new avenue to improve the current density of electrocatalytic performance of CO_2RR via integration of D–A heterojunction units into framework materials for the beneficial of electron transfer ability.

4. Experimental Section

Materials: All chemicals and solvents were purchased without further purification. Thieno[3,2-*b*]thiophene-2,5-dicarboxaldehyde (TT) was purchased from HWRK CHEM, $\text{Co}(\text{OAc})_2 \cdot 4\text{H}_2\text{O}$ (98%) was purchased from Alfa, pyrrole (99%) was purchased from Adamas, benzyl alcohol (99%) was purchased from Macklin. Chlorobenzene, *o*-dichlorobenzene, dioxane, DMF, acetic acid, NaOAc, and K_2CO_3 were purchased from Sinopharm Chemical Reagent Co., Ltd., Carbon fabric, LION Ketjenblack (ECP600)D.

Synthesis of 5,10,15,20-tetrakis(4-aminophenyl)porphinatocobalt(II) (Co-TAPP): Co-TAPP was synthesized according to reference.^[23] TAPP (200 mg, 0.30 mmol) and NaOAc (108 mg, 1.3 mmol) were added mixed solution with 45 mL of DMF and 63 mL of chlorobenzene, then Co(OAc)₂·4H₂O (147 mg, 0.59 mmol) was added. After equipping with a Soxhlet apparatus with a paper thimble containing K₂CO₃ (1.1 g, 8.0 mmol), reaction mixture was stirred under nitrogen at reflux for 24 h. Upon cooling, the Soxhlet apparatus was replaced with a distillation setup, and the solvent was removed under vacuum. The dark solid was suspended in CHCl₃ (100 mL), then solvent was removed through vacuum filtration. The crude product was then washed thoroughly with water three times, saturate NaHCO₃ solution one time, and then water again three times. The resulting dark purple microcrystalline powder was dried under high vacuum overnight.

Synthesis of TT-Por(Co)-COF: Thieno[3,2-b]thiophene-2,5-dicarboxaldehyde (TT) (7.84 mg, 0.04 mmol) and Co-TAPP (14.62 mg, 0.02 mmol) were added to a Pyrex tube measuring 10 × 8 mm (o.d × i.d) and dispersed in a solvent mixture of benzyl alcohol, *o*-dichlorobenzene and 6 M acetic acid (15:5:2 v:v:v). After sonication for 10 min the tube was flash frozen at 77 K and flame sealed. Then the reaction was heated at 120 °C and kept for 3 days, the precipitate was separated by filtration, and transferred to a Soxhlet extractor and washed thoroughly with dioxane (12 h) and acetone (12 h). Finally, the product was evacuated at 120 °C under dynamic vacuum.

Synthesis of TT-Por(2H)-COF: TT-Por(2H)-COF was prepared under the similar conditions of TT-Por(Co)-COF with TAPP as monomer instead of Co-TAPP.^[47]

Synthesis of COF-366-Co: COF-366-Co was synthesized according to ref. [23].

Electrochemical Measurements: The electrochemical tests were performed in a standard three-electrode configuration using H-type cell separated by an anion exchange membrane (Nafion-117) by chi700e at room temperature. One compartment contained 70 mL 0.5 M KHCO₃ electrolyte and Pt foil as counter electrodes, another with Ag/AgCl electrode as reference electrode and catalyst-modified carbon fabric electrode as work electrode. 5 mg of the catalyst and 1.7 mg ketjenblack were dispersed in 1 mL of isopropanol, and 40 μL of Nafion (5 wt%) under sonication for 2 h to form homogeneous ink. 80 μL ink was loaded onto the carbon fabric electrode with 1 × 1 cm². During the electrochemical tests, the 0.5 M KHCO₃ was purged with Ar or CO₂ for 30 min to achieve the Ar-saturated or CO₂-saturated solution. LSV was tested with a scan rate of 10 mV s⁻¹ from 0 to -1.0 V versus RHE. All tested potentials were converted to RHE scale using the following equation: $E_{(vs\ RHE)} = E_{(vs\ Ag/AgCl)} + 0.059\ pH + 0.197\ V$ (pH = 7.2). The gas phase composition was analyzed by Gas Chromatograph.

Faradaic Efficiency Calculation for CO:

$$FE = \frac{J_{CO}}{J_{total}} = \frac{\nu_{CO} \times N \times F}{J_{total}} \quad (1)$$

where J_{CO} is the partial current density of CO; J_{total} is the total current density; N is the number of electron transferred for product formation, in which it was two for CO; ν_{CO} is the production rate of CO (tested by GC); F is the Faradaic constant, 96 485 C mol⁻¹; FE is the Faradaic efficiency for CO production.

Evaluation of TOF (h⁻¹) for CO:

$$TOF = \frac{I_{product}/NF}{m_{cat} \times \omega/M_{metal}} \times 3600 \quad (2)$$

$I_{product}$ is the partial current of CO; m_{cat} is the catalyst mass in the electrode, g; ω is the metal loading in catalyst; M_{metal} is the atomic mass of metal.

The Nyquist plots were obtained by the EIS test which was conducted by applying AC voltage with 5 mV amplitude in frequency range from 100 mHz to 100 kHz. DPV was tested in acetonitrile, with 0.1 M tetrabutylammonium hexafluorophosphate as electrolyte and 0.1 mM ferrocene as internal reference, Pt wires as the counter

electrode, Ag/AgCl as reference electrode, and glassy carbon electrode as work electrode. The potential window was from 0 up to 1.4 V with a modulation amplitude of 0.005 V, modulation time of 0.05 s, and an interval time of 0.5 s.

Supporting Information

Supporting Information is available from the Wiley Online Library or from the author.

Acknowledgements

Q.W. and M.-J.M. contributed equally to this work. The authors thank Dr. Guan-E Wang from Prof. Gang Xu's group for conductivity measurements, and thank Dr. Cheng-Min Ji from Prof. Jun-Hua Luo's group for testing the carrier mobility of materials. The authors acknowledge the financial support from the National Key Research and Development Program of China (2018YFA0208600 and 2018YFA0704502); NSFC (21871263, 21671188, and 21520102001); Key Research Program of Frontier Science, CAS (QYZDJ-SSW-SLH045); Strategic Priority Research Program of the Chinese Academy of Sciences (XDB20000000); Youth Innovation Promotion Association, CAS (Y201850). The authors acknowledge the beamline BL14W1 station for XAFS measurements at the Shanghai Synchrotron Radiation Facility, China.

Conflict of Interest

The authors declare no conflict of interest.

Keywords

CO₂ electrocatalysis, cobalt, covalent organic frameworks, donor-acceptor, porphyrin

Received: August 12, 2020

Revised: September 2, 2020

Published online:

- [1] F. M. Mota, D. H. Kim, *Chem. Soc. Rev.* **2019**, *48*, 205.
- [2] A. Vasileff, C. C. Xu, Y. Jiao, Y. Zheng, S. Z. Qiao, *Chem* **2018**, *4*, 1809.
- [3] D. Yang, B. Ni, X. Wang, *Adv. Energy Mater.* **2020**, *10*, 2001142.
- [4] C. T. Dinh, T. Burdyny, M. G. Kibria, A. Seifitokaldani, C. M. Gabardo, F. P. G. de Arquer, A. Kiani, J. P. Edwards, P. De Luna, O. S. Bushuyev, C. Q. Zou, R. Quintero-Bermudez, Y. J. Pang, D. Sinton, E. H. Sargent, *Science* **2018**, *360*, 783.
- [5] C. H. Yang, S. Y. Li, Z. C. Zhang, H. Q. Wang, H. L. Liu, F. Jiao, Z. G. Guo, X. T. Zhang, W. P. Hu, *Small* **2020**, *16*, 2001847.
- [6] M. Balamurugan, H. Y. Jeong, V. S. K. Choutipalli, J. S. Hong, H. Seo, N. Saravanan, J. H. Jang, K. G. Lee, Y. H. Lee, S. W. Im, V. Subramanian, S. H. Kim, K. T. Nam, *Small* **2020**, *16*, 2000955.
- [7] E. Boutin, L. Merakeb, B. Ma, B. Boudy, M. Wang, J. Bonin, E. Anxolabehere-Mallart, M. Robert, *Small* **2020**, *49*, 5772.
- [8] Y. H. Wang, J. L. Liu, Y. F. Wang, A. M. Al-Enizi, G. F. Zheng, *Small* **2017**, *13*, 1701809.
- [9] S. Nitopi, E. Bertheussen, S. B. Scott, X. Y. Liu, A. K. Engstfeld, S. Horch, B. Seger, I. E. L. Stephens, K. Chan, C. Hahn, J. K. Nørskov, T. F. Jaramillo, I. Chorkendorff, *Chem. Rev.* **2019**, *119*, 7610.

- [10] D. F. Gao, R. M. Arán-Ais, H. S. Jeon, B. R. Cuenya, *Nat. Catal.* **2019**, *2*, 198.
- [11] Y. Hou, Y. B. Huang, Y. L. Liang, G. L. Chai, J. D. Yi, T. Zhang, K. T. Zang, J. Luo, R. Xu, H. Lin, S. Y. Zhang, H. M. Wang, R. Cao, *CCS Chem* **2019**, *1*, 384.
- [12] X. G. Li, S. B. Xi, L. B. Sun, S. Dou, Z. F. Huang, T. Su, X. Wang, *Adv. Sci.* **2020**, *7*, 2001545.
- [13] Y. Hou, Y. L. Liang, P. C. Shi, Y. B. Huang, R. Cao, *Appl. Catal., B* **2020**, *271*, 118929.
- [14] J. Gu, C. S. Hsu, L. C. Bai, H. M. Chen, X. L. Hu, *Science* **2019**, *364*, 1091.
- [15] J. Y. Han, P. F. An, S. H. Liu, X. F. Zhang, D. W. Wang, Y. Yuan, J. Guo, X. Y. Qiu, K. Hou, L. Shi, Y. Zhang, S. L. Zhao, C. Long, Z. Y. Tang, *Angew. Chem., Int. Ed.* **2019**, *58*, 12711.
- [16] Y. R. Wang, Q. Huang, C. T. He, Y. F. Chen, J. Liu, F. C. Shen, Y. Q. Lan, *Nat. Commun.* **2018**, *9*, 4466.
- [17] Z. F. Xin, Y. R. Wang, Y. F. Chen, W. L. Li, L. Z. Dong, Y. Q. Lan, *Nano Energy* **2020**, *67*, 104233.
- [18] R. Hinogami, S. Yotsuhashi, M. Deguchi, Y. Zenitani, H. Hashiba, Y. Yamada, *ECS Electrochem. Lett.* **2012**, *1*, H17.
- [19] N. Kornienko, Y. B. Zhao, C. S. Kley, C. H. Zhu, D. Kim, S. Lin, C. J. Chang, O. M. Yaghi, P. D. Yang, *J. Am. Chem. Soc.* **2015**, *137*, 14129.
- [20] I. Hod, M. D. Sampson, P. Deria, C. P. Kubiak, O. K. Farha, J. T. Hupp, *ACS Catal.* **2015**, *5*, 6302.
- [21] B. An, Z. Li, Y. Song, J. Z. Zhang, L. Z. Zeng, C. Wang, W. B. Lin, *Nat. Catal.* **2019**, *2*, 709.
- [22] H. X. Zhong, M. Ghorbani-Asl, K. H. Ly, J. C. Zhang, J. Ge, M. C. Wang, Z. Q. Liao, D. Makarov, E. Zschech, E. Brunner, I. M. Weidinger, J. Zhang, A. V. Krashennikov, S. Kaskel, R. H. Dong, X. L. Feng, *Nat. Commun.* **2020**, *11*, 1409.
- [23] S. Lin, C. S. Diercks, Y. B. Zhang, N. Kornienko, E. M. Nichols, Y. B. Zhao, A. R. Paris, D. Kim, P. D. Yang, O. M. Yaghi, C. J. Chang, *Science* **2015**, *349*, 1208.
- [24] X. Zhu, C. C. Tian, H. H. Wu, Y. Y. He, L. He, H. Wang, X. D. Zhuang, H. L. Liu, C. G. Xia, S. Dai, *ACS Appl. Mater. Interfaces* **2018**, *10*, 43588.
- [25] C. L. Yao, J. C. Li, W. Gao, Q. Jiang, *Chem. - Eur. J.* **2018**, *24*, 11051.
- [26] S. Huang, D. D. Chen, C. Meng, S. J. Wang, S. Ren, D. M. Han, M. Xiao, L. Y. Sun, Y. Z. Meng, *Small* **2019**, *15*, 1904830.
- [27] J. Q. Dong, X. Han, Y. Liu, H. Y. Li, Y. Cui, *Angew. Chem. Int. Ed.* **2020**, *59*, 13722.
- [28] E. M. Johnson, R. Haiges, S. C. Marinescu, *ACS Appl. Mater. Interfaces* **2018**, *10*, 37919.
- [29] C. S. Diercks, S. Lin, N. Kornienko, E. A. Kapustin, E. M. Nichols, C. H. Zhu, Y. B. Zhao, C. J. Chang, O. M. Yaghi, *J. Am. Chem. Soc.* **2018**, *140*, 1116.
- [30] N. Huang, K. H. Lee, Y. Yue, X. Y. Xu, S. Irle, Q. H. Jiang, D. L. Jiang, *Angew. Chem., Int. Ed.* **2020**, *132*, 16730.
- [31] Y. S. Li, Q. Chen, T. T. Xu, Z. Xie, J. J. Liu, X. Yu, S. Q. Ma, T. S. Qin, L. Chen, *J. Am. Chem. Soc.* **2019**, *141*, 13822.
- [32] S. Z. Wang, X. Y. Xu, Y. Yue, K. S. Yu, Q. J. Shui, N. Huang, H. Z. Chen, *Small Str.* **2020**, <https://doi.org/10.1002/sstr.202000021>.
- [33] H. Y. Liu, J. Chu, Z. L. Yin, X. Cai, L. Zhuang, H. X. Deng, *Chem* **2018**, *4*, 1696.
- [34] P. L. Cheung, S. K. Lee, C. P. Kubiak, *Chem. Mater.* **2019**, *31*, 1908.
- [35] M. Dogru, M. Handloser, F. Auras, T. Kunz, D. Medina, A. Hartschuh, P. Knochel, T. Bein, *Angew. Chem., Int. Ed.* **2013**, *52*, 2920.
- [36] G. H. V. Bertrand, V. K. Michaelis, T. C. Onga, R. G. Griffin, M. Dinca, *Proc. Natl. Acad. Sci. USA* **2013**, *110*, 4923.
- [37] L. Ascherl, T. Sick, J. T. Margraf, S. H. Lapidus, M. Calik, C. Hettstedt, K. Karaghiosoff, M. Döblinger, T. Clark, K. W. Chapman, F. Auras, T. Bein, *Nat. Chem.* **2016**, *8*, 310.
- [38] H. Yang, S. L. Zhang, L. L. Han, Z. Zhang, Z. Xue, J. Gao, Y. J. Li, C. S. Huang, Y. P. Yi, H. B. Liu, Y. L. Li, *ACS Appl. Mater. Interfaces* **2016**, *8*, 5366.
- [39] H. Li, J. H. Chang, S. S. Li, X. Y. Guan, D. H. Li, C. Y. Li, L. X. Tang, M. Xue, Y. S. Yan, V. Valtchev, S. L. Qiu, Q. R. Fang, *J. Am. Chem. Soc.* **2019**, *141*, 13324.
- [40] D. H. Li, C. Y. Li, L. J. Zhang, H. Li, L. K. Zhu, D. J. Yang, Q. R. Fang, S. L. Qiu, X. D. Yao, *J. Am. Chem. Soc.* **2020**, *142*, 8104.
- [41] P. Pachfule, A. Acharjya, J. Roeser, R. P. Sivasankaran, M. Y. Ye, A. Brückner, J. Schmidta, A. Thomas, *Chem. Sci.* **2019**, *10*, 8316.
- [42] W. B. Chen, L. Wang, D. Mo, F. He, Z. L. Wen, X. J. Wu, H. G. Xu, L. Chen, *Angew. Chem., Int. Ed.* **2020**, *59*, 16902.
- [43] T. W. Kim, S. H. Jun, Y. Ha, R. K. Yadav, A. Kumar, C. Y. Yoo, I. Oh, H. K. Lim, J. W. Shin, R. Ryoo, H. Kim, J. Kim, J. O. Baeg, H. Ihee, *Nat. Commun.* **2019**, *10*, 1873.
- [44] T. Joshi, C. Chen, H. F. Li, C. S. Diercks, G. Q. Wang, P. J. Waller, H. Li, J. L. Bredas, O. M. Yaghi, M. F. Crommie, *Adv. Mater.* **2019**, *31*, 1805941.
- [45] H. J. Zhu, M. Lu, Y. R. Wang, S. J. Yao, M. Zhang, Y. H. Kan, J. Liu, Y. F. Chen, S. L. Li, Y. Q. Lan, *Nat. Commun.* **2020**, *11*, 497.
- [46] M. S. Liao, S. Scheinera, *J. Chem. Phys.* **2002**, *117*, 205.
- [47] N. Keller, M. Calik, D. Sharapa, H. R. Soni, P. M. Zehetmaier, S. Rager, F. Auras, A. C. Jakowetz, A. Gorling, T. Clark, T. Bein, *J. Am. Chem. Soc.* **2018**, *140*, 16544.
- [48] N. Li, W. Y. Lu, K. Peib, W. X. Chen, *RSC Adv.* **2015**, *5*, 9374.
- [49] J. D. Yi, R. Xu, G. L. Chai, T. Zhang, K. T. Zang, B. Nan, H. Lin, Y. L. Liang, J. Q. Lv, J. Luo, R. Si, Y. B. Huang, R. Cao, *J. Mater. Chem. A* **2019**, *7*, 1252.
- [50] Q. Wu, R. K. Xie, M. J. Mao, G. L. Chai, J. D. Yi, S. S. Zhao, Y. B. Huang, R. Cao, *ACS Energy Lett.* **2020**, *5*, 1005.
- [51] J. M. Frost, M. A. Faist, J. Nelson, *Adv. Mater.* **2010**, *22*, 4881.
- [52] Y. M. Liu, H. Hou, Y. Z. Zhou, X. J. Zhao, C. Tang, Y. Z. Tan, K. Müllen, *Nat. Commun.* **2018**, *9*, 1901.
- [53] Y. S. Wu, Z. Jiang, X. Lu, Y. Y. Liang, H. L. Wang, *Nature* **2019**, *575*, 639.
- [54] B. H. Solis, A. G. Maher, D. K. Dogutan, D. G. Nocera, S. Hammes-Schiffer, *Proc. Natl. Acad. Sci. USA* **2016**, *113*, 485.
- [55] A. G. Maher, M. Liu, D. G. Nocera, *Inorg. Chem.* **2019**, *58*, 7958.